Cell Reports
Physical Science

Article

Scalable and oil-free fabrication of monodisperse microgels via all-aqueous microfluidics

Graphical abstract

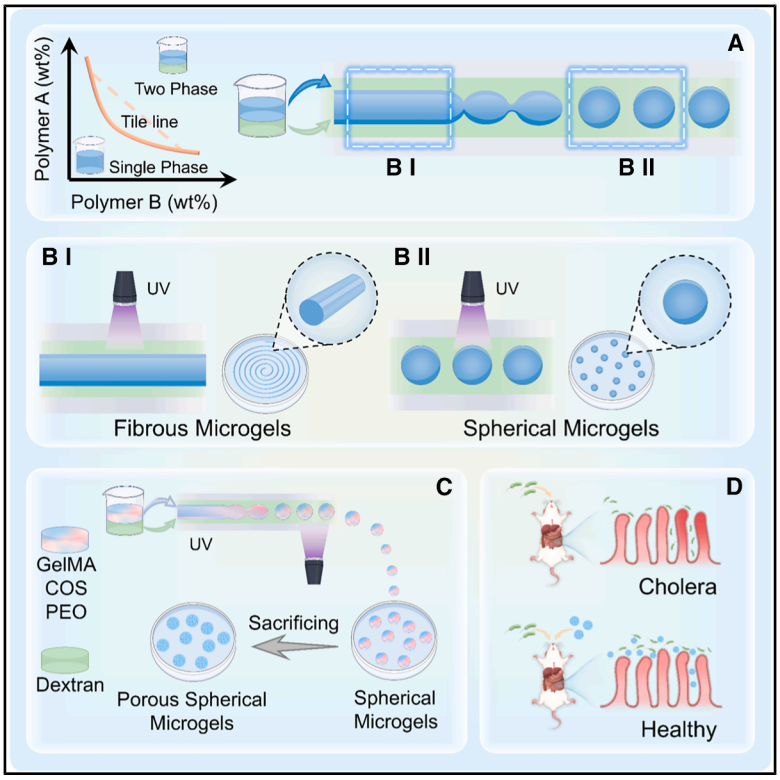

Highlights

- Oil-free ATPS microfluidics enables scalable monodisperse microgels
- Stable droplet formation occurs without valves or oscillation
- Morphology and size are tuned via flow and curing position
- COS-loaded GelMA microgels suppress *V. cholerae in vivo*

Authors

Jialin Wu, Long Chen, Changyi Xiao, ..., Lingran Du, Maobin Xie, Guosheng Tang

Correspondence

guoshengtang@gzhmu.edu.cn

In brief

Wu et al. present an oil-free ATPS microfluidics platform that generates monodisperse, structurally tunable microgels without valve control. The system supports diverse biomaterials and demonstrates therapeutic efficacy of COS-loaded GelMA microgels against *Vibrio cholerae* infection.

Wu et al., 2026, Cell Reports Physical Science 7, 103253
April 15, 2026
https://doi.org/10.1016/j.xcrp.2026.103253

CellPress

Cell Reports
Physical Science

CellPress
OPEN ACCESS

Article

Scalable and oil-free fabrication of monodisperse microgels via all-aqueous microfluidics

Jialin Wu,[1,5] Long Chen,[1,2,5] Changyi Xiao,[1,5] Leyan Xuan,[1,5] Lijie Chen,[1] Lili Wu,[1] Xudong Qin,[1] Yutao Liu,[4] Zhuo Jiang,[3] Lingran Du,[1] Maobin Xie,[2] and Guosheng Tang[1,6,*]

[1]Guangzhou Municipal and Guangdong Provincial Key Laboratory of Molecular Target and Clinical Pharmacology, the NMPA and State Key Laboratory of Respiratory Disease, School of Pharmaceutical Sciences and the Fifth Affiliated Hospital, Guangzhou Medical University, Guangzhou 511436, China

[2]The Fourth Affiliated Hospital of Guangzhou Medical University, School of Biomedical Engineering, Guangzhou Medical University, Guangzhou 511436, China

[3]College of Food Science, South China Agricultural University, Guangzhou 510642, China

[4]School of Life Sciences, Faculty of Medicine, Tianjin University, Tianjin 300072, China

[5]These authors contributed equally

[6]Lead contact

*Correspondence: guoshengtang@gzhmu.edu.cn

https://doi.org/10.1016/j.xcrp.2026.103253

SUMMARY

While traditional microfluidics approaches achieve considerable success in microgel production, surfactant- and oil-free fabrication of monodisperse microgels remains challenging. Here, we present a simple one-step strategy that uses water-in-water (W/W) aqueous two-phase systems (ATPSs) to enable scalable production of monodisperse microgels without surfactants or oils. This approach leverages the low interfacial tension of ATPSs and provides precise control over microgel size, morphology, and porosity by tuning phase flow rates, pre-gel compositions, and nozzle configurations. We demonstrate versatility by fabricating diverse microgels (e.g., gelatin methacryloyl, hyaluronic acid methacryloyl, Pluronic F127 diacrylate, and sericin), indicating broad material compatibility. The oil- and surfactant-free process ensures high cytocompatibility. As a proof of concept, we engineer porous gelatin methacryloyl (GelMA) microgels loaded with chitosan oligosaccharides, which inhibit *Vibrio cholerae* growth, suggesting potential for cholera prevention and broader biomedical applications.

INTRODUCTION

Microgels, composed of crosslinked polymer networks and typically ranging from tens to hundreds of micrometers in diameter, exhibit high water content, excellent biocompatibility, and tunable physicochemical properties.[1,2] In recent years, they have garnered significant attention in tissue engineering and regenerative medicine.[3–5] Compared to conventional bulk hydrogels, microgels exhibit notable structural and functional advantages. Their high surface area-to-volume ratio and shortened diffusion paths enable more efficient transport of nutrients and metabolic waste, markedly enhancing long-term cell viability.[6,7] Through specific assembly strategies, microgels can be organized into interconnected three-dimensional porous structures. These structures not only enhance cell infiltration and tissue formation but also enable precise emulation of complex tissue microarchitectures by tailoring particle size, shape, mechanical properties, and bioactive agent incorporation.[8–10] Beyond regenerative applications, microgels and microspheres have been widely investigated as drug delivery carriers for bacterial infections and gastrointestinal diseases.[11,12] Porous structures and microenvironment-associated cues can improve local therapeutic performance, and protective "armoring" designs can enhance oral delivery and intestinal retention of biotherapeutics such as probiotics. These considerations underscore the importance of simultaneously engineering carrier composition and micro-architecture to achieve robust protection and controlled release under complex physiological conditions. Accordingly, fabrication methods that enable monodisperse microgels with tunable structures in a biocompatible manner are highly desirable for translational drug delivery.

Droplet microfluidics, a powerful platform for microgel fabrication, exploits fluid immiscibility to engineer monodisperse particles with tunable size and morphology.[13,14] By dispersing a hydrogel precursor solution (e.g., alginate or poly(ethylene glycol) diacrylate [PEGDA]) into an immiscible oil phase, this technique generates highly uniform droplets that can be crosslinked *in situ* to form microspheres with precise control over payload encapsulation.[15] By manipulating microfluidic parameters, such as flow rates and junction configurations, the size and shape of microspheres can be precisely tailored for specific biomedical applications.[16] Furthermore, the low equipment requirements of

microfluidics contribute to reduced production costs.[17] However, since most hydrogel droplets are generated in a water-in-oil (W/O) system, a washing step is needed to eliminate adhered oil. This can be particularly problematic for microgels containing cells, as the washing process is cumbersome, and the use of surfactants may adversely affect cell viability.[18]

To address the limitations associated with conventional W/O emulsion methods, recent studies have explored alternative strategies, notably the aqueous two-phase system (ATPS)-based approach.[19,20] This water-in-water (W/W) system is formed by spontaneous phase separation of an aqueous mixture containing two incompatible hydrophilic components, typically polymers or polymer-salt combinations, above critical concentrations.[21,22] Unlike traditional W/O systems, ATPSs possess several attractive features for microgel fabrication. First, both phases of an ATPS have high water content, significantly enhancing biocompatibility by eliminating the need for oils.[23] Additionally, the ATPS closely resembles physiological microenvironments, providing more relevant conditions for biomedical applications. However, the interfacial tension of aqueous-aqueous interfaces within ATPSs is extremely low, on the order of 10^{-4}–10^{-1} mN m^{-1}, several orders of magnitude lower than typical W/O interfaces.[24] This ultralow interfacial tension complicates stable droplet formation in conventional microfluidic platforms, often necessitating the incorporation of valve control systems.[19,25,26] These external valve control devices not only add complexity to the fabrication setup but also increase operational difficulties, potentially affecting the scalability of production. Moreover, the reliance of these technologies on alginate, either as the sole component or as a mandatory element of bioinks in most ATPS-based systems, further limits their flexibility and material versatility.[27] Despite alginate (Alg)'s desirable mechanical robustness, its inherent stiffness can restrict cell spreading, adhesion, and proliferation, limiting effective tissue integration and repair.[28]

To overcome the limitations, we developed a droplet microfluidic strategy based on ATPSs for fabricating uniform and structurally controllable microgels. In this approach, GelMA, a photo-crosslinkable gelatin derivative widely used for constructing 3D tissue scaffolds due to its cytocompatibility, biodegradability, inherent bioactivity, and tunable physical properties,[28,29] serves as the exemplary dispersed phase, while dextran, a natural hydrophilic polysaccharide with excellent biocompatibility and processability,[30] functions as the continuous phase. Compared with traditional W/O emulsion systems, the ATPS-based microfluidics approach eliminates the need for organic solvents, significantly enhancing biocompatibility and simplifying the fabrication process. Notably, unlike most current ATPS-based microfluidics approaches that rely on external valve control systems to achieve droplet formation under ultralow interfacial tension, our method generates stable droplets without auxiliary control mechanisms. By precisely tuning phase concentrations and flow parameters, we achieved size-controllable GelMA microgels. Furthermore, spatial modulation of the ultraviolet (UV) curing location enables flexible shape control, curing upstream yields fibers, whereas downstream curing results in spherical carriers. Porous microgels can be fabricated by incorporating a porogen aqueous phase within the GelMA solution, and Janus microgels can be prepared by introducing multiple dispersed phases. This platform also offers broad material versatility, with demonstrated compatibility for fabricating microcarriers from various hydrogel materials, including hyaluronic acid methacryloyl (HAMA), Pluronic F127 diacrylate (F127-DA), and sericin (SS). These advantages position our strategy as a promising tool for customizable biofabrication, precision medicine, and advanced regenerative therapies. Our previous research found that Alg microgels loaded with chitosan oligosaccharide (COS) demonstrated effective prevention and treatment of cholera.[31] However, the properties of Alg resulted in a short *in vivo* retention time for the microspheres. Here, porous spherical GelMA microgels loaded with COS were prepared using optimized ATPS-based microfluidics, successfully extending the *in vivo* retention time of the drug and achieving promising prevention and treatment outcomes (Figure 1).

In summary, the development of this ATPS-based microfluidics strategy represents a significant advancement in microgel fabrication, successfully overcoming the fundamental limitations inherent to traditional W/O systems and valve-dependent devices in ATPS-based systems, offering unprecedented versatility in material selection and microgel morphology. This technology not only streamlines the all-aqueous production of microgels but also enhances material compatibility and processing flexibility while significantly expanding potential application domains. The demonstrated biomedical potential is particularly noteworthy—these advantages make the platform especially suitable as a biocarrier, with the capability to revolutionize multiple biomedical fields, including advanced drug delivery systems, tissue engineering, and regenerative medicine. As a prime example, porous spherical GelMA microgels encapsulating COS demonstrated significant efficacy in both preventing and treating cholera infection.

RESULTS AND DISCUSSION

Fabrication of microgels with one-step ATPS-based microfluidics

The strategy of utilizing ATPS-based microfluidics without organic phases offers significant advantages, particularly in terms of biocompatibility. In this study, we describe a straightforward method for preparing microgels, including spherical and fibrous microgels, employing an ATPS by actively disturbing the interface of the aqueous two-phase flow. The device employed for microgel fabrication consists of four main components: a digital syringe pump, a homemade coaxial nozzle system, a collecting bath, and a movable UV light source (Figure S1). The coaxial nozzle system is assembled from two needles with different diameters through which the continuous and dispersed phase of the ATPS is separately introduced (Figure S2). Typically, dextran, a highly biocompatible medium, was selected as the continuous phase, with gentle hydrostatic pressure applied to the flowing GelMA phase, facilitating the formation of microgels with low interfacial tension, free from external disturbances (Figure 2A). Of note, compared to previous W/W microfluidics systems,[19,25,26] our strategy eliminates the need for external valve control or oscillation, relying instead on

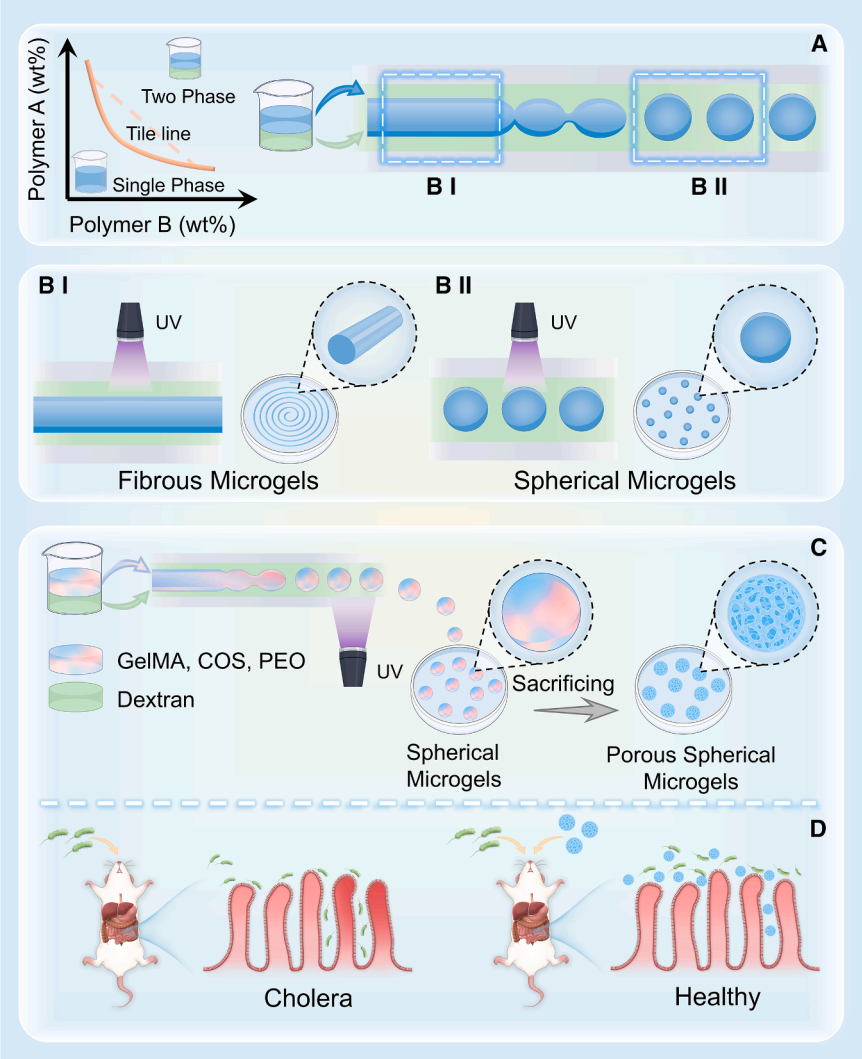

Figure 1. Development of ATPS droplet microfluidics strategy and its application in cholera treatment and prevention

(A) Phase diagram of ATPS and schematic of the microgel fabricated using the ATPS-based microfluidics strategy.

(B) By modulating the UV curing position within the microfluidic channel, the ATPS-based microfluidics platform enables precise spatiotemporal control over microgel morphology (B_I, fibrous; B_{II}, spherical) and architecture.

(C and D) Schematic of the preparation of porous spherical GelMA microgels loaded with COS (C) and its application in cholera treatment and prevention (D).

stable interface construction and flow-driven jetting for droplet formation. This significantly simplifies device design and enhances operational stability.

The formation of microgels within the ATPS-based microfluidics device predominantly occurs through a viscosity-dominated jetting mechanism, characterized by the competition between viscous stresses and interfacial tension at the two-phase interface.[32,33] The observed experimental phenomena suggest a flow condition in which the viscous drag force exerted by the continuous phase significantly surpasses the stabilizing force from interfacial tension. This is consistent with conditions where the capillary number (Ca_c), defined as $Ca_c = \frac{\mu_c \upsilon_c}{\Upsilon}$ (with μ_c, υ_c, and Υ representing the continuous-phase viscosity, velocity, and interfacial tension, respectively), approaches or exceeds unity. In representative combinations, the flow rate of the continuous phase (dextran-rich solution) is much higher than that of the dispersed phase (GelMA-rich solution), usually greater than 10:1. Under these circumstances, the high flow rate of the continuous phase exerts a stretching effect on the dispersed-phase jet through viscous shear, resulting in a gradual narrowing of the jet diameter, which is typical of narrowing jet characteristics.

Subsequently, this narrowing jet undergoes breakup into droplets via Rayleigh-Plateau instability, where disturbances at the fluid interface amplify progressively until discrete droplets detach. From a theoretical viewpoint, the diameter of this jet (d_{jet}) can be reasonably estimated by relating it to the microfluidic channel diameter (ω_o) and the flow rate ratio (ϕ) between dispersed and continuous phases, following the scaling law: $\frac{d_{jet}}{\omega_o} = \sqrt{\frac{\phi}{2}}$.[34,35] Furthermore, the size of droplets formed from the breakup of this jet is determined by the most unstable wavelength (λ_ω) of the jet instability. Based on classic hydrodynamic instability theory, the final droplet diameter (D) can be quantitatively described as $\frac{D}{d_{jet}} = \left(\frac{3\pi}{2k^*}\right)^{1/3}$, where k^* represents the dimensionless wavenumber dictated by the Tomotika dispersion relation, which incorporates the viscosity contrast between the dispersed and continuous phases.[32]

To evaluate the feasibility of this method, we first fabricated spherical GelMA microgels using the custom-designed ATPS microfluidics device. For real-time visualization of droplet formation, GelMA was fluorescently labeled with fluorescein isothiocyanate (FITC). As illustrated in Figures 2B–2D and S3, we systematically captured the dispersion and formation of microdroplets within the microchannel. Upon co-injection of GelMA and dextran solution through a custom coaxial needle into the microfluidic channel, uniform fiber bundles were initially observed (Figure 2B). These bundles subsequently underwent Rayleigh-Plateau instability-induced rupture at the midsection of the microchannel, gradually transitioning into bead-like intermediate structures (Figure 2C). Eventually, complete shear separation between the GelMA and dextran phases resulted in the

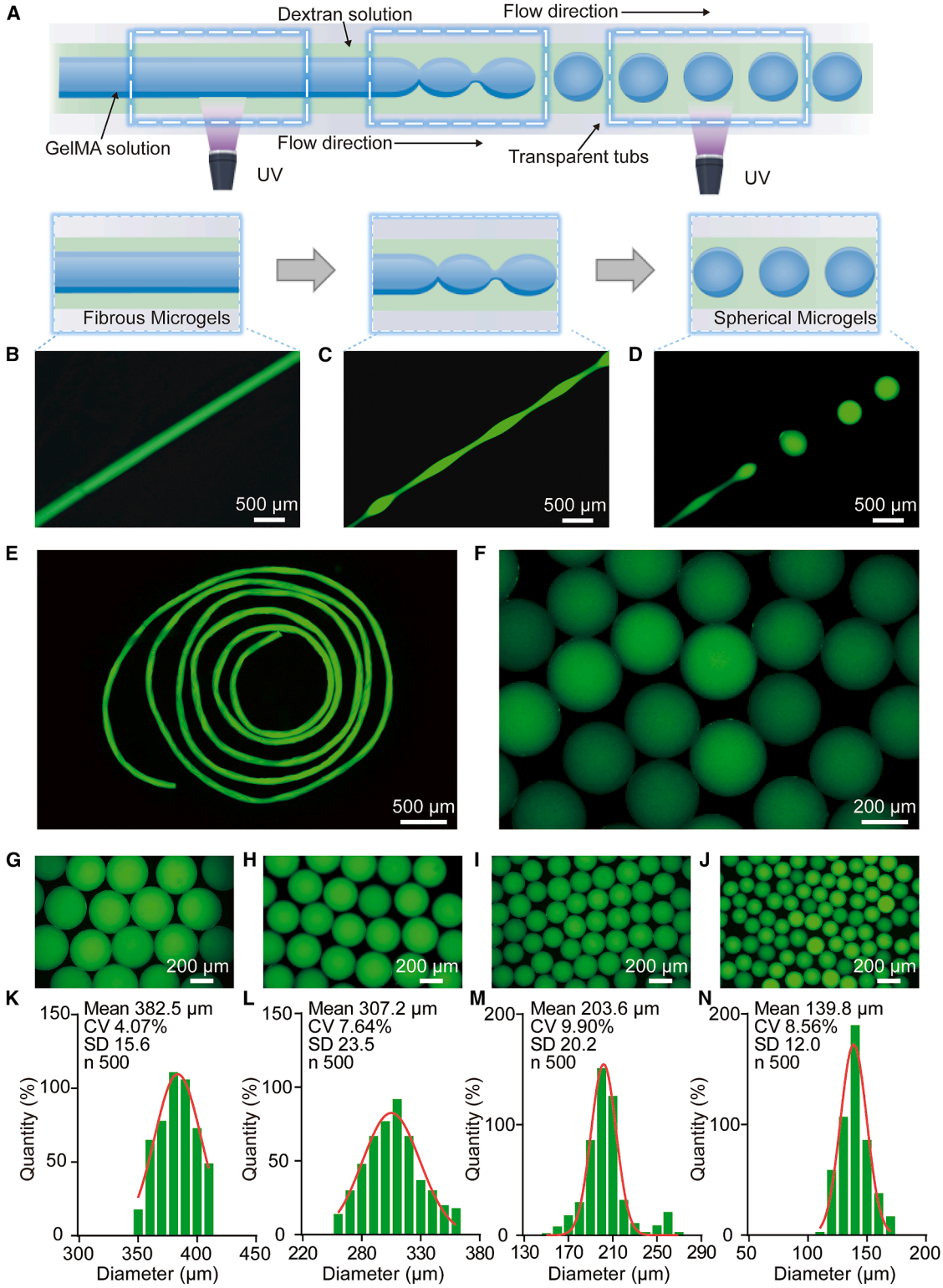

Figure 2. ATPS droplet microfluidics system

(A) Schematic of the ATPS droplet microfluidics system for the fabrication of GelMA microgel.

(B–D) Real-time fluorescence images of GelMA microgel formation within the microchannel corresponding to the schematic. Scale bars: 200 μm.

(legend continued on next page)

formation of well-defined, uniformly sized spherical GelMA droplets (Figure 2D; Video S1). By precisely controlling the spatial position of UV irradiation during crosslinking, we successfully fabricated both spherical and fibrous GelMA microgels (Figures 2E and 2F). This morphological tunability enhances not only the flexibility of the preparation process but also expands the potential application scope of the resulting microgels. Compared to conventional methods, this approach streamlines the fabrication workflow while enabling efficient and reproducible control over microstructure geometry tailored to specific biomedical needs.

To further assess the size controllability of spherical GelMA microgels, we systematically adjusted the flow parameters of both continuous and dispersed phases. As shown in Figures 2G–2J, S4, and S5, the spherical GelMA microgels' diameter decreased with an increase in the flow rate of the continuous phase and increased with a rise in the flow rate of the dispersed phase. Additionally, by varying the diameter of the custom coaxial nozzle, we achieved further control over particle size distribution (Figure S6). Through these combined strategies, we were able to produce spherical GelMA microgels with diameters ranging from 77 to 710 μm, exhibiting exceptionally low polydispersity (Figures 2K–2N). In summary, these results validate the feasibility and versatility of the ATPS-based microfluidics platform for fabricating morphologically tunable, size-controllable GelMA microgels. The ability to rapidly produce both spherical and fibrous structures with precise dimensional control offers a robust and adaptable solution for diverse biofabrication applications, particularly in drug screening, tissue engineering, and advanced cellular models.

Morphological customization of microgels

To further demonstrate the versatility and adaptability of the ATPS-based microfluidics strategy, we systematically explored its capability to fabricate spherical microgels with alternative morphologies, including homogeneous, porous, and Janus spherical microgels. We first assessed the feasibility of fabricating homogeneous spherical GelMA microgels using the ATPS-based microfluidics approach. Optical microscopy confirmed that the resulting GelMA microsphere exhibited highly regular spherical shapes with consistent diameters and low polydispersity (Figure 3A). Moreover, the obtained GelMA microspheres were smooth and wrinkle free, which could be attributed to the absence of external mechanical disturbances during droplet formation, aside from weak hydrostatic pressures arising from the controlled flow rate differentials between the two-phase solutions (Figures 3B and S7).

The inherent characteristics of the ATPS provides substantial advantages for fabricating porous microspheres without introducing additional fabrication steps. Specifically, porous GelMA microspheres could be readily generated by using a co-mixed solution of GelMA and polyethylene oxide (PEO) as the dispersed phase, with PEO as the sacrificial component. Upon UV-induced photo-crosslinking, the acrylate groups in GelMA underwent free-radical polymerization, forming a stable crosslinked network, while PEO remained uncrosslinked and could subsequently be removed through washing. The formation of porous GelMA microspheres was confirmed in Figures 2C and 2D, which presented a clear and homogeneous porous structure under scanning electron microscopy (SEM) observation. To further reinforce the structural characterization beyond qualitative SEM observations, we quantitatively evaluated the degradation and swelling behaviors of the porous GelMA microgels (Figure S8). As shown in Figure S8A, the porous GelMA microgels exhibited a progressive decrease in relative weight during degradation, with ~70% remaining on day 3 and ~33% remaining by day 7. Moreover, the microgels displayed rapid swelling within the first few hours and then gradually approached a plateau (Figure S8B), reaching ~300% at 24 h.

Furthermore, to assess whether ATPS-based microfluidics could generate anisotropic microspheres, we designed a coaxial nozzle featuring two inner needles (Figure S1). As presented in Figure 3E, Janus GelMA microspheres were successfully fabricated from GelMA-PEO mixtures loaded with red and green fluorescent nanoparticles simply by adjusting the nozzle configuration. These Janus microspheres not only preserved their porous internal structure but also displayed sharply defined internal boundaries separating the two compartments, confirming successful physical compartmentalization within each individual microsphere (Figure 3F).

As previously discussed, the ATPS-based microfluidics approach provides facile access to fibrous microgels by precisely controlling the spatial location of UV crosslinking. To further highlight the versatility of this strategy, we investigated the straightforward yet precise tunability of fibrous GelMA microgel dimensions by varying several key parameters, including the continuous aqueous phase flow rate, dispersed aqueous flow rate, and concentration of the inner or outer solution. As shown in Figures 3G–3U, GelMA microfibers with diameters ranging from 30 to 900 μm were successfully fabricated by easily adjusting these parameters. This level of dimensional control highlights the flexibility and precision offered by the ATPS microfluidics platform for fabricating both spherical and fibrous microgels with customized architectures.

Broad material adaptability in microgel fabrication

Although microgel fabrication strategies utilizing ATPS offer notable advantages, including high biocompatibility and simplified processing, existing research predominantly focuses on specific biomaterials, and the generalizability and robustness of ATPS-based microfluidics approaches across different biomaterials remain inadequately explored. To extend the applicability and versatility of the ATPS-based microfluidics strategy, we sought to determine whether this method could reliably generate microgels from a broad range of biomaterials. Here,

(E and F) Selective preparation of fibrous microgel (E) and spherical microgel (F). Scale bars, 500 μm. (F) Prepared by adjusting different curing positions within the microchannel. Scale bars: 200 μm.

(G–N) Spherical GelMA microgels (G–J) with a wide range of diameters (from 130 to 400 μm) and low polydispersity. Scale bars, 200 μm. Those in (K–N) can be produced using the ATPS droplet microfluidic strategy. The flow rates of the continuous phase (dextran) were 10, 20, 30, and 50 μL min^{-1}, while the flow rate of the dispersed phase (GelMA) was consistently 1 μL min^{-1}. Data are presented as the percentage of microgels falling within each diameter range.

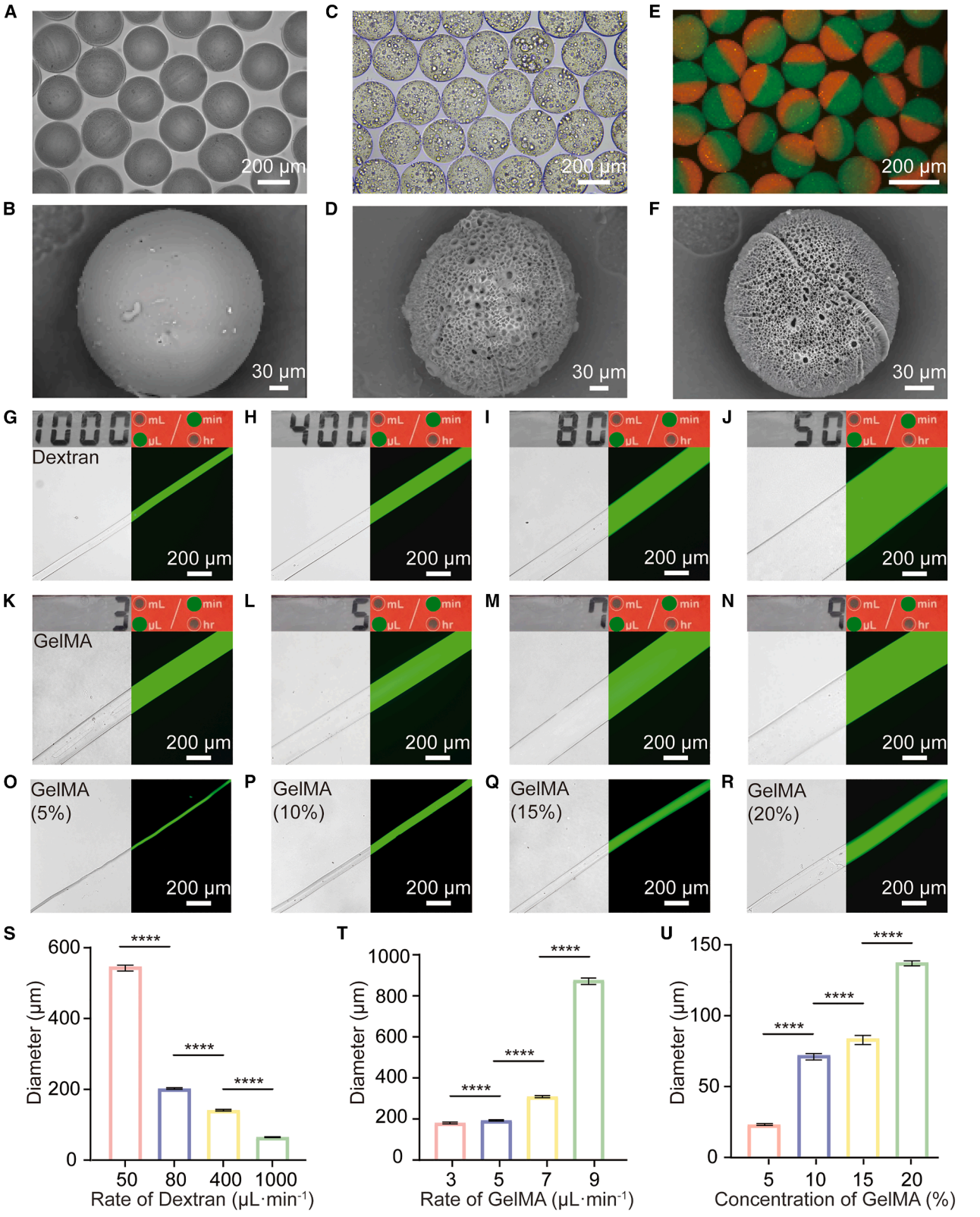

(legend on next page)

we selected several representative biocompatible polymers, including GelMA, HAMA, SS, and F127-DA, encompassing natural polysaccharides, block copolymers, and protein-based biomaterials (Figure 4A). Prior to microgel fabrication, we first constructed detailed phase diagrams to precisely characterize the phase separation behavior of each biomacromolecule-dextran combination under varying concentrations and compositional ratios (Figures 4B–4E; Videos S2–S5). These phase diagrams revealed the phase separation behavior and miscibility characteristics of each system under specific conditions, offering crucial theoretical guidance for optimizing microgel preparation and enhancing reproducibility.

Using dextran as the continuous phase, we systematically fabricated both spherical and fibrous microgels by introducing GelMA, HAMA, SS, or F127-DA as dispersed phase materials within the ATPS microfluidics device. Under identical fabrication conditions, each combination successfully formed stable and uniformly shaped microgels (Figures 4F–4U). Interestingly, although consistent production parameters were maintained across all combinations, we observed clear variations in final microgel dimensions among different hydrogels. These differences in size can likely be attributed to inherent variations in solution viscosity and surface tension between distinct biomaterial solutions, influencing the droplet breakup and shear separation dynamics within the microfluidic channel. These results collectively confirm our initial hypothesis, clearly demonstrating the exceptional adaptability and versatility of the ATPS-based microfluidic strategy across multiple biomaterial systems. Such versatility and reliability substantially broaden the potential utility of this approach, making it highly promising for diverse biomedical applications such as drug delivery, cell encapsulation, and regenerative medicine.

Cellular behaviors

To evaluate the biocompatibility of the microgels generated using our approach and further demonstrate their suitability for biomedical applications, we next selected GelMA as a representative biomaterial to investigate the ability of microgels to support cell survival, proliferation, and morphological integrity in a three-dimensional microenvironment. To test this, we co-cultured three representative cell types (A549 cells, HeLa cells, and human umbilical vein endothelial cells [HUVECs]) with spherical GelMA microgels and monitored their biological behavior over a 7-day culture period; cell viability and proliferation were evaluated by Live/Dead assay and Cell Counting Kit-8 (CCK-8), respectively. As shown in Figures 5A–5C (cells cultured without microspheres, defined as the control group), Figures 5D–5F (cells cultured with porous GelMA microspheres, defined as the porous GelMA microspheres [PGM] group), as well as Figure S9, Live/Dead staining across three representative cell lines demonstrated consistently high viability with negligible cell death over 1, 4, and 7 days. Quantitative viability analysis further corroborated these observations, with all cell lines maintaining survival rates exceeding 99.8% at all time points (Figures 5G–5I), confirming that the GelMA microgel interface supported a cytocompatible environment. In parallel, CCK-8 assays revealed a progressive increase in metabolic activity for all three cell lines over time, with absorbance values rising approximately 8-fold by day 7 relative to day 1 (Figures 5J–5L). This continuous growth trend indicates that the microgels not only maintained cell viability but also actively supported cellular proliferation and metabolic function. These findings collectively demonstrate that spherical GelMA microgels fabricated via the ATPS-based microfluidics platform offer a stable, non-cytotoxic, and bioactive interface capable of sustaining a variety of cells in a three-dimensional co-culture setting.

We subsequently expanded our demonstration in a cell behavioral assay by further illustrating the unique biological relevance of spherical GelMA microgels generated by ATPS-based microfluidics strategies. As discussed, current ATPS-based strategies for microgel fabrication have been limited to a few specific biomaterials, which significantly constrains the range of potential applications for the resulting microcarriers. Specifically, sodium Alg (Na-Alg) has remained as a widely used material for microgel fabrication in microfluidics strategies due to its fast physical crosslinking mechanism. Nevertheless, Alg cannot easily interact with the cells. Therefore, Alg would mostly function like a solid wall that constrains cell movement and remodeling, as well reported by others.[36] To investigate the biological relevance and functional performance of microgels fabricated using this platform, HUVECs were directly encapsulated in spherical GelMA microgels during microfluidic formation. These embedded cells maintained a survival rate of up to 99.9% (Figure S10), indicating that the ATPS environment and photopolymerization process did not negatively impact cell health. To further verify the spreading and morphologies of the HUVECs encapsulated in spherical GelMA and Na-Alg microgels, F-actin staining was performed. As revealed in Figures 5M, 5N, and S11, cells in contact with spherical GelMA microgels displayed well-organized cytoskeletal structures and clear spreading behavior, in contrast to cells cultured with spherical Na-Alg microgels, which remained rounded and exhibited limited cytoskeletal development. These results highlight the superior performance of GelMA microgels in supporting cell adhesion and mimicking the natural extracellular matrix by offering both mechanical support and biochemical cues essential for maintaining cellular integrity and function.

Figure 3. ATPS droplet microfluidics strategy enables precise customization of microgel morphology

(A–F) Microscope and SEM images of homogeneous (A and B), porous (C and D), and Janus (E and F) spherical microgels produced by the ATPS-based microfluidics strategy. Homogeneous microspheres were obtained using a pure GelMA solution as the dispersed phase, whereas porous microspheres were produced with a blended GelMA/PEO solution, with PEO acting as the sacrificial component. Janus porous microspheres were further distinguished by incorporating fluorescent dyes of different colors. Scale bars in (A), (C), (E) represent 200 μm and in (B), (D), (F) 30 μm.

(G–R) Representative images showing the tunability of microfiber diameters by adjusting various parameters: continuous-phase (dextran) flow rates of 1,000, 400, 80, and 50 μL min^{-1} (G–J); dispersed-phase (GelMA) flow rates of 3, 5, 7, and 9 μL min^{-1} (K–N); and dispersed-phase GelMA concentrations of 5, 10, 15, and 20 wt % (O–R). Scale bars: 200 μm.

(S–U) Quantitative analysis of the corresponding microfiber diameters. Significance was determined by one-way ANOVA and is indicated as the p value. ****$p < 0.0001$. Data are presented as mean ± SD.

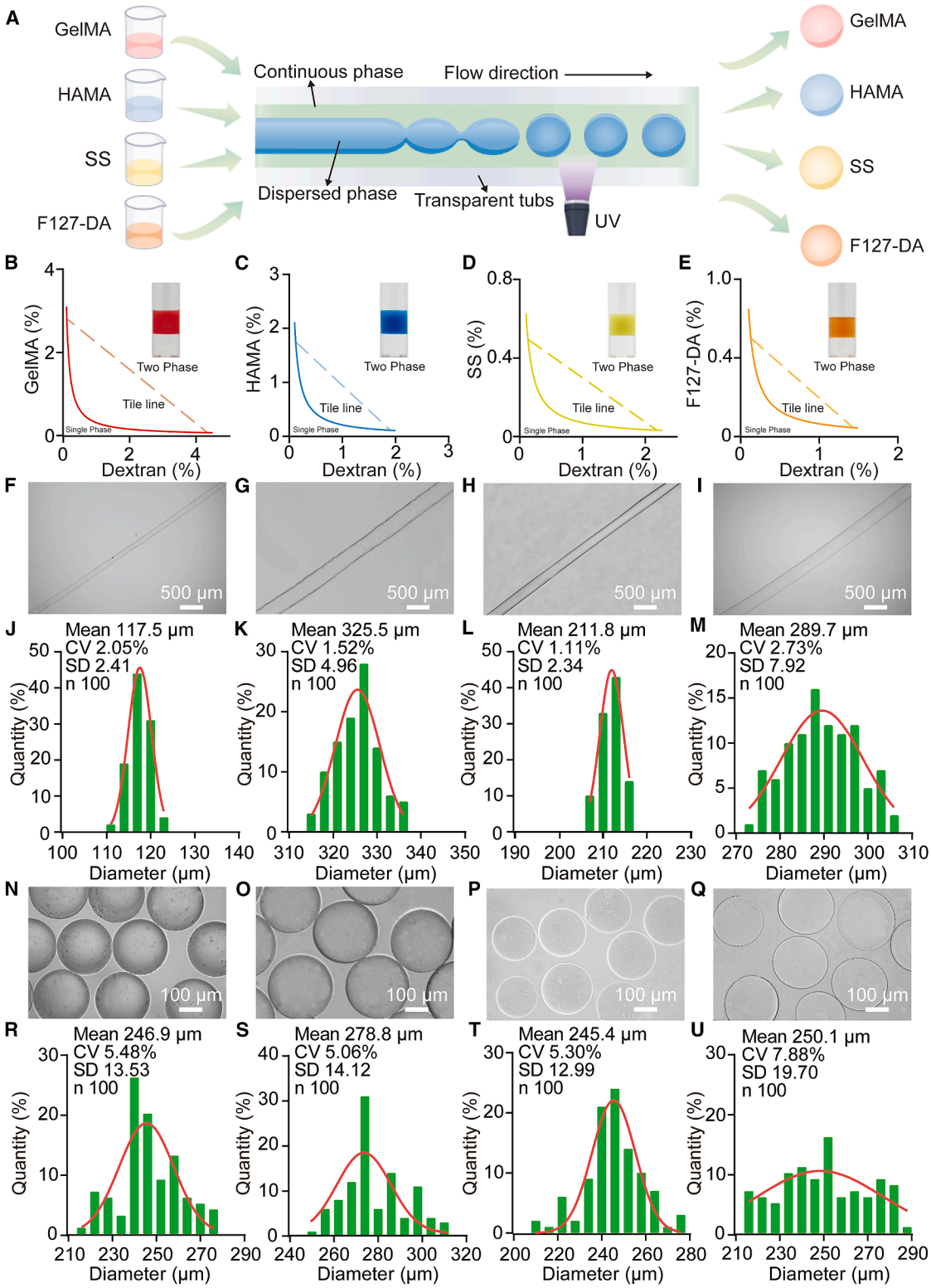

(legend on next page)

Application of COS-loaded porous microspheres in cholera prevention and treatment

In our previous studies, we demonstrated that COS exhibits potent anti-virulence effects against *Vibrio cholerae* infection. While COS-loaded Alg microspheres show efficacy in reducing bacterial colonization, their therapeutic potential is limited by the rapid clearance of Alg-based carriers *in vivo* due to their pH-responsive properties.[31] To overcome these limitations and demonstrate the potential of ATPS droplet microfluidics strategies for tailored drug delivery and tissue engineering applications, we innovatively used COS-loaded porous GelMA microspheres (CPGMs) for cholera control. To assess their *in vivo* effectiveness, an established adult mouse model was employed to investigate whether CPGMs could reduce the virulence of *V. cholerae* (Figure 6A). First, in order to verify the hypothesis that GelMA microspheres could successfully overcome the extreme conditions in the gastric environment to reach the intestine, an investigation of their dissolution behavior was conducted in simulated gastric fluid (SGF) and simulated intestinal fluid (SIF). As shown in Figure 6B, the CPGMs remained structurally intact in SGF, demonstrating excellent acid resistance and stability. In contrast, gradual swelling and degradation were observed in SIF, with the microspheres nearly fully dissolved by 48 h. To quantify COS release kinetics, UV-visible (UV-vis) spectrophotometry was performed (Figure 6C). The results showed negligible COS release in SGF, while the COS concentration in SIF increased over time, reaching nearly 100% of the encapsulated drug by 48 h. These findings suggest that GelMA microspheres effectively protect COS from gastric degradation and prolong its retention time in the intestinal environment. To evaluate the biocompatibility of CPGMs, Caco-2 cells were used to assess cell viability[37] after culturing with either the non-microsphere group or the CPGM group for 147 days (Figure S12A and S12B), followed by statistical analysis (Figure S12C). The results showed no significant cytotoxicity, indicating good biocompatibility. Further *in vivo* retention studies were conducted using an *in vivo* imaging system (IVIS) following oral administration. As shown in Figure 6F, GelMA microspheres could be detected in the small intestine 2 h after administration and were completely eliminated in the ileum and colon at 48 h, demonstrating prolonged retention. Notably, the intensity of the fluorescence gradually decreased over time, indicating a slow and controlled degradation of the CPGMs. Compared with COS-loaded Alg microspheres,[31] which exhibited rapid clearance and limited gastrointestinal retention, the CPGMs prepared via the ATPS strategy showed significantly prolonged residence in the intestine. This enhanced retention behavior offers a distinct therapeutic advantage by reducing the required frequency of administration and enhancing both treatment efficacy and patient compliance.

To evaluate the effect of CPGMs on *V. cholerae* intestinal colonization, an adult mouse colonization model was employed following established protocols.[31] As shown in Figure 6D, CPGM treatment significantly reduced the bacterial burden in the small intestine compared with untreated controls, whereas the porous GelMA microsphere group without COS loading (PGM group) showed no significant difference, indicating that the carrier alone does not affect colonization.

To further elucidate the mechanism, the expression of key virulence genes (*tcpA*, *tcpP*, *toxR*, and *toxT*) was analyzed. As shown in Figure 6E, quantitative reverse-transcription PCR (RT-qPCR) results revealed a marked downregulation of these genes in the CPGM-treated group, while no significant changes were observed in the PGM group. These results indicate that CPGM inhibits *V. cholerae* colonization primarily by suppressing virulence gene expression.

To further investigate the mechanism, small intestine tissue samples were subjected to immunofluorescence staining for key inflammatory cytokines[38,39] (tumor necrosis factor alpha [TNF-α], green; interleukin-1β [IL-1β], red; nuclei, blue). As shown, the fluorescence intensity in the CPGM-treated group was significantly lower compared to both the PGM and cholera groups, where the fluorescence intensity remained high, indicating elevated inflammation (Figures 7A–7C). To validate the therapeutic efficacy of CPGMs against *V. cholerae* infection, hematoxylin and eosin (H&E) staining and pathological scoring of mouse small intestinal tissues were performed. The H&E staining results revealed significant inflammation and severe villus damage in the intestines of the untreated group and PGM group (Figures 7D and 7E). In contrast, mice treated with CPGMs exhibited markedly reduced tissue damage and a well-preserved villus structure (Figure 7F). Moreover, histological scoring indicated significantly lower scores in the CPGM group compared to the control group and PGM group, providing additional confirmation of the therapeutic effect of CPGMs (Figure S13). Collectively, these findings suggest that GelMA microspheres effectively protect COS from gastric degradation and enable its accumulation in the intestinal tract, inhibiting *V. cholerae* colonization *in vivo*.

DISCUSSION

In this study, we demonstrate that an ATPS-based droplet microfluidics platform enables the robust fabrication of GelMA microgels, overcoming key limitations of conventional W/O emulsion methods. This approach enables precise control over microgel size, shape, and porosity while eliminating harmful solvents—key advantages for tissue engineering and therapeutic agent delivery. Moreover, the platform's versatility extends to other biomaterials, including HAMA, SS, and F127-DA,

Figure 4. The ATPS-based microfluidics strategy offers broad material adaptability

(A) The wide material adaptability of the ATPS preparation strategy.

(B–E) Phase diagram of ATPS comprising dextran with GelMA (B), HAMA (C), SS (D), and F127-DA (E). The bimodal curve is delineated as the critical boundary between the single-phase regimen and the two-phase regimen. An initial point in the two-phase regimen phase separates into two thermal equilibrium aqueous phases, the dextran-rich phase and another phase, following a tie line.

(F–U) Microfibers (F–I) and microspheres (N–Q) fabricated by corresponding ATPS combinations and their size distribution (J–M and R–U). Scale bars in (F–I) represent 500 μm and in (N–Q) 100 μm. Data are presented as the percentage of microgels falling within each diameter range.

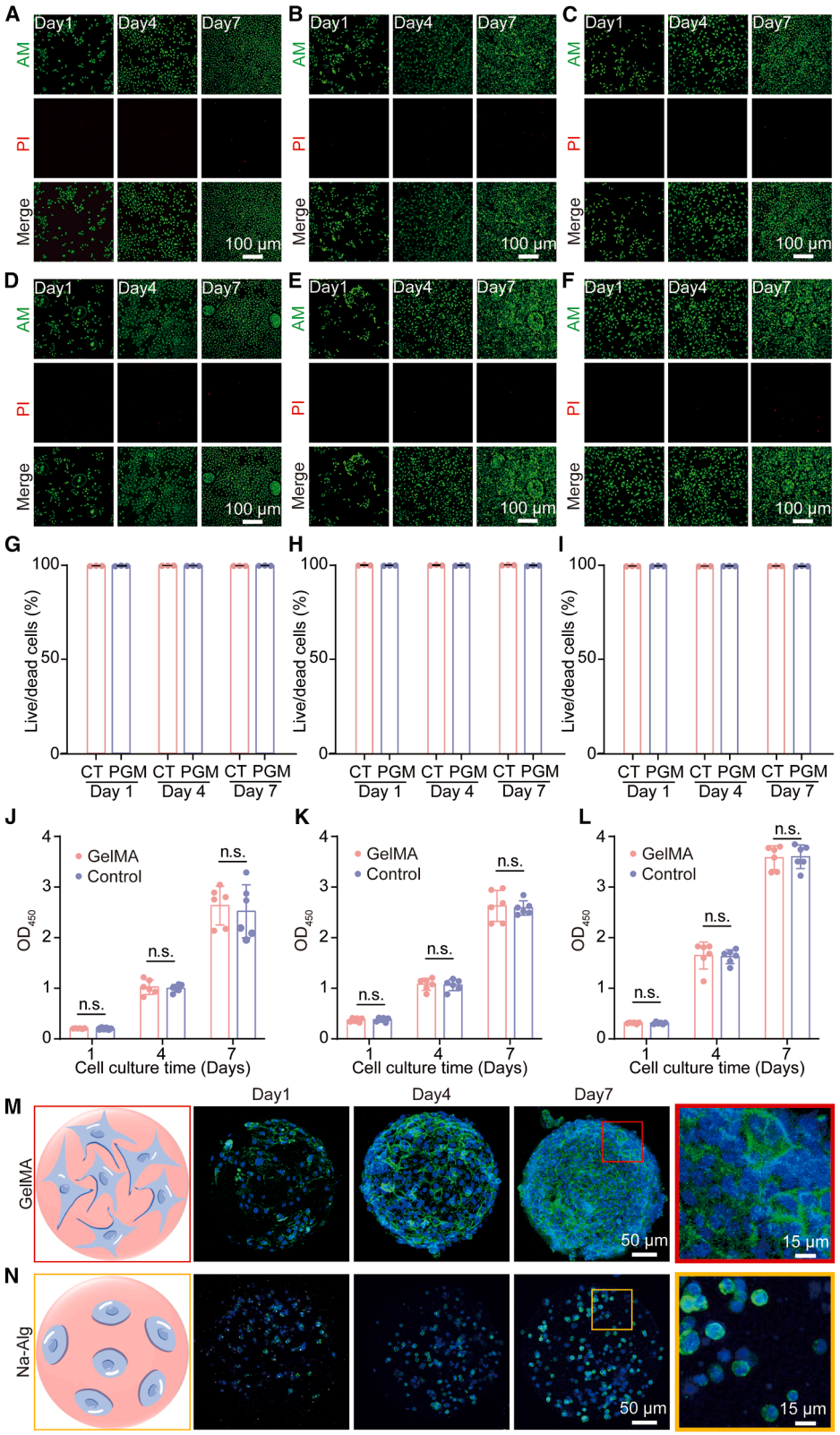

(legend on next page)

demonstrating broad material selectivity for tailoring microcarrier properties to diverse therapeutic and regenerative needs. This flexibility significantly expands the method's applicability across biomedical fields.

In conventional W/O emulsion systems for hydrogel droplet generation, extensive washing steps are required to remove residual oil, which may compromise the biocompatibility of the microcarriers. In contrast, our ATPS-based method eliminates the use of organic solvents, preserving cell viability and enhancing biocompatibility. By utilizing biocompatible aqueous phases such as GelMA and dextran, our approach not only avoids residual oil contamination but also enables the production of stable microcarriers over a broad concentration range. This tunability is crucial for engineering microcarriers with tailored mechanical properties, including adjustable stiffness and degradation rates, to meet specific therapeutic needs.

Our ATPS-based microfluidics platform enables precise spatiotemporal control over microgel morphology and architecture. By modulating the UV curing position within the microfluidic channel, we achieve on-demand fabrication of spherical, fibrous, and hybrid microstructures, significantly expanding the structural repertoire of microgels. Furthermore, the introduction of a porogen phase into the shear phase generates porous spherical GelMA microgels with tunable pore size and distribution. Moreover, by manipulating the number of shear phases within the microfluidic setup, our method facilitates the production of complex, multifunctional microspheres with varied morphologies. This versatile strategy unlocks opportunities for designing advanced bio-microcarriers with application-specific functionalities in drug delivery, tissue engineering, and beyond.

Although several studies have attempted to replace oil phases with all-aqueous systems as the continuous phase, critical bottlenecks—such as dependence on complex valve modulation, limited material compatibility, and poor scalability—remain unresolved. These limitations hinder the development of versatile, scalable, and structurally tunable microcarriers. In contrast, our ATPS droplet microfluidics strategy addresses these limitations by leveraging the low interfacial tension between aqueous phases to achieve robust droplet generation via a viscosity-dominated jetting mechanism. Instead, we leverage stable interface construction within a coaxial flow device, significantly simplifying device fabrication and operation while enhancing control over microgel morphology. Furthermore, our method accommodates a wider range of biomaterials, including GelMA, HAMA, SS, and F127-DA, without compromising the structural integrity of the generated microgels. This versatility effectively decouples microgel design from specific material and morphology constraints. Additionally, the successful fabrication of porous and Janus microspheres further underscores the versatility of our system, offering opportunities for multifunctional biomedical applications such as multistage drug release and complex tissue interfaces.

Furthermore, the study highlighted the advantages of our ATPS-based method in extending the *in vivo* retention time of drug-loaded microspheres. The GelMA microspheres, when loaded with COS, demonstrated significantly improved therapeutic outcomes compared to Alg-based microspheres, which typically suffer from rapid *in vivo* clearance. This improved retention can lead to better therapeutic efficacy, particularly in chronic conditions where sustained release is critical.

Although the ATPS-based microfluidics approach for microgel fabrication holds significant potential, several challenges remain. The relatively low interfacial tension in aqueous systems makes droplets more susceptible to external disturbances in microfluidic channels, which may affect microsphere uniformity and production scalability when compared with conventional oil-based approaches. Therefore, further optimization of flow rates, phase compositions, and channel designs is required to improve droplet formation consistency and scalability. In conclusion, the droplet microfluidics method utilizing ATPS for GelMA microcarriers presents a highly adaptable and biocompatible approach for fabricating hydrogel microspheres with tunable properties. This method not only overcomes the limitations of traditional W/O emulsions but also enhances the versatility and effectiveness of microgel carriers, advancing their application in tissue engineering, regenerative medicine, and drug or cell delivery.

METHODS

Synthesis of GelMA

GelMA was synthesized following previously established protocols.[1,2] Briefly, porcine skin gelatin (type A, ~300 g bloom, weight-average molecular weight [Mw] ~90 kDa, Sigma-Aldrich) was dissolved in phosphate-buffered saline (PBS) at 10% (w/v) under constant stirring at 50°C. Methacrylic anhydride (MAA; Sigma-Aldrich) was added dropwise via syringe pump to a final concentration of 5% (v/v), and the reaction was allowed to proceed for 2 h at 50°C. The mixture was diluted 2-fold with warm PBS and dialyzed against deionized (DI) water at 40°C for 7 days using dialysis tubing (molecular weight cut-off [MWCO] 12–14 kDa, Spectrum Chemical). Water was changed every 12 h. The dialyzed solution was filtered through a 0.22-μm Stericup-GP vacuum filtration system (Millipore), aliquoted (25 mL per vial), frozen at −80°C for 24 h,

Figure 5. Biocompatibility of microgels prepared by ATPS droplet microfluidics strategy

(A–C) Quantitative analysis of cell proliferation in the control group (A549 cells, HeLa cells, and HUVECs) after 1, 4, and 7 days of culture, evaluated by CCK-8 assay.

(D–F) Quantitative analysis of cell proliferation in the PGM group (A549 cells, HeLa cells, and HUVECs) after 1, 4, and 7 days of culture, evaluated by CCK-8 assay. Scale bars: 100 μm.

(G–L) Live/Dead staining images (G–I) and their corresponding quantitative cell viability analyses (J–L) of different cell lines co-cultured with GelMA microspheres for 1, 4, and 7 days.

(M and N) Vinculin immunofluorescence staining observed by CLSM for HUVECs cultured on GelMA (M) and Na-Alg (N) microspheres for 1, 4, and 7 days. Scale bars represent 50 μm and in the boxed area 15 μm. Significance was determined by two-way ANOVA and is indicated by the p value. n.s., $p > 0.05$. Data are presented as mean ± SD.

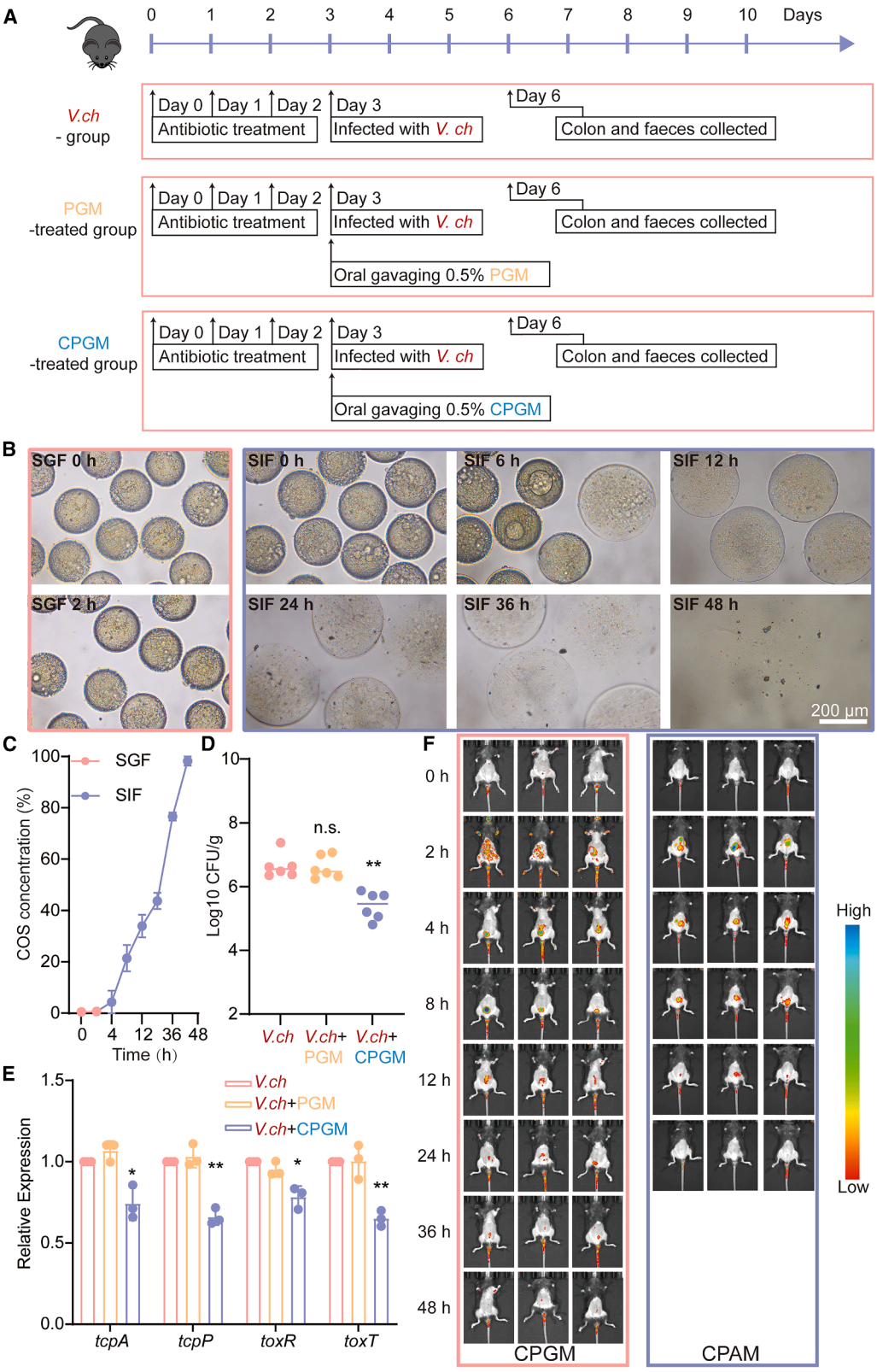

(legend on next page)

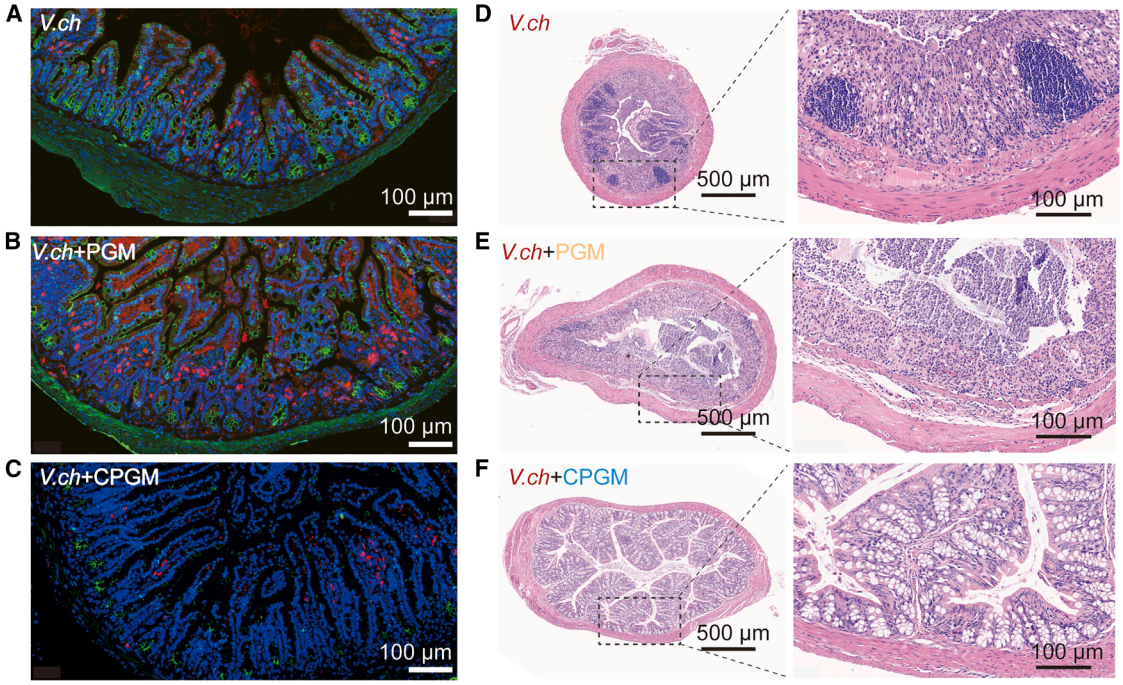

Figure 7. CPGMs reduce cholera-associated intestinal inflammation

(A–C) Immunofluorescence dual staining of the small intestine from control, PGM, and CPGM groups, showing TNF-α (green), IL-1β (red), and nuclei (blue). Scale bars: 100 μm.

(D–F) H&E staining of *V. cholerae* in the small intestine of adult mice administered 0.5% PGMs or CPGMs. All analyses were performed 3 days post infection. Scale bars represent 500 μm and in the boxed area 100 μm.

and lyophilized for 5 days (FreeZone, Labconco) to obtain GelMA in dry form. HAMA was prepared by dissolving hyaluronic acid (1% w/v) in DI water, adjusting the pH to 8.0, and slowly adding MAA (1% v/v) on ice. The reaction proceeded for 4 h with continuous pH adjustment, followed by dialysis (3.5 kDa MWCO) and lyophilization.

Synthesis of FITC-labeled GelMA

To label GelMA with fluorescein, 1 g of GelMA was dissolved in 30 mL of 1 M 2-(N-morpholino)ethanesulfonic acid (MES) buffer (pH 7.4). A stock solution of fluorescein isothiocyanate–poly(-ethylene glycol)–N-hydroxysuccinimide (FITC-PEG-NHS) (Nanocs) was prepared by dissolving 100 mg of the compound in 1 mL of dimethyl sulfoxide (DMSO). A 2.37-μL volume of FITC-PEG-NHS was added to the GelMA solution and allowed to react for 2 h in the dark at room temperature. The mixture was dialyzed (MWCO 12–14 kDa) at room temperature for 5 days and then lyophilized.

Preparation of GelMA bioinks

GelMA was dissolved in DI water at 37°C for 1 h to a final concentration of 6.0%, 8.0%, 10.0%, or 12.0% (w/v). A 0.3% (w/v) concentration of lithium phenyl-2,4,6-trimethylbenzoylphosphinate (LAP; Sigma-Aldrich) photoinitiator was added to enable cross-linking upon UV exposure (10 mW/cm^2, 360–480 nm, 30 s). Unless otherwise stated, bioinks used in subsequent experiments consisted of 10% GelMA and 0.3% photoinitiator. All bioinks were stored at 4°C until use.

Synthesis of HAMA

HAMA was synthesized via *trans*-esterification between MAA and sodium hyaluronate (Mw ~1,500 kDa, HAworks). Four

Figure 6. GelMA microspheres loaded with COS to control *V. cholerae* colonization

(A) Schematic of the *V. cholerae* colonization infection model.

(B) Dissolution of COS-loaded GelMA microspheres in SGF and SIF. Scale bars: 200 μm.

(C) The release of COS in SGF and SIF detected by UV spectrophotometer.

(D) Evaluation of the colonization ability of *V. cholerae* in the small intestine of adult mice administered PGM and CPGMs at the time of bacterial oral challenge 3 days post infection (n = 7).

(E) RT-qPCR expression levels of virulence genes (*tcpP*, *toxT*, *ctxA*, and *tcpA*) of *V. cholerae* in the small intestine of adult mice administered 0.5% PGM or CPGM 24 h post infection (n = 3).

(F) The retention time of CPGMs and CPAMs (COS-loaded porous Alg microspheres) in mice detected by IVIS. Scale bars represent 500 μm and in the boxed area 100 μm. Significance was determined by a two-sided Mann-Whitney U test or two-tailed unpaired Student's t test and is indicated as the p value. *p < 0.05, **p < 0.01, ***p < 0.001. Data are presented as mean ± SD.

grams of hyaluronic acid was dissolved in 200 mL of DI water at 4°C overnight. The solution was chilled on ice, and 133.3 mL of dimethylformamide (DMF) was added under vigorous stirring. MAA (7.88 mL) was introduced slowly over 4 h using a syringe pump. During this period, pH was maintained above 8.5 using an automated titrator (Mettler DL21, Mettler-Toledo) dispensing 0.5 M NaOH. The reaction continued for an additional 18 h at 4°C. Sodium chloride was added to a final concentration of 0.5 M, and the product was precipitated in 10 volumes of cold ethanol at −78°C. The precipitate was collected, redissolved in DI water, dialyzed against DI water (MWCO 12–14 kDa, Visking), and lyophilized. HAMA was characterized by ^{1}H-NMR (Bruker Avance II 300 MHz).

Preparation of HAMA bioinks

HAMA was dissolved in DI water at 2.0% (w/v) at room temperature overnight. LAP was added at 0.3% (w/v), and the solution was stored at 4°C. Photocrosslinking was performed under UV irradiation (10 mW/cm^2, 360–480 nm, 30 s) during use.

Synthesis of SS

SS was extracted from *Bombyx mori* cocoons following a standard hot water degumming method. Briefly, raw silk cocoons (Soochow Silk, China) were cut into small pieces and boiled in DI water at 100°C for 60 min at a material-to-liquid ratio of 1:50 (w/v). The resulting SS-rich solution was filtered through double-layer gauze to remove undissolved fibroin and debris. The filtrate was centrifuged at 8,000 × *g* for 20 min at 4°C to eliminate particulate matter. The supernatant was collected and dialyzed (MWCO 12–14 kDa, Spectrum Chemical) against DI water for 3 days at 4°C, with water replaced every 8 h. After dialysis, the SS solution was filtered through a 0.22-μm vacuum filtration unit (Millipore), aliquoted, frozen at −80°C overnight, and lyophilized for 3 days (Labconco FreeZone). The resulting powder was stored at −20°C until use. The purified SS was characterized by UV-vis spectrophotometry and SDS-PAGE to confirm protein integrity and purity.

Preparation of SS bioinks

SS powder was dissolved in sterile DI water at 37°C to obtain final concentrations of 2.0%, 4.0%, and 6.0% (w/v). The solution was stirred gently for 2 h to ensure complete dissolution. To enable photocrosslinking, 0.5 mM tris(2,2′-bipyridyl)ruthenium(II) chloride ($Ru(bpy)_3Cl_2$) and 10 mM sodium persulfate ($Na_2S_2O_8$) were added to the SS solution and mixed until fully dissolved. The bioinks were then filtered through a 0.22-μm sterile vacuum filtration unit (Millipore), aliquoted, and stored at 4°C until further use. UV crosslinking was performed using a 10 mW cm^{-2} light source (360–480 nm) for 30 s unless otherwise specified.

GelMA, HAMA, and SS were synthesized in house and used directly without further purification. PEO was obtained from Sigma-Aldrich, while F127-DA was purchased from Engineering for Life. COS and dextran (500 kDa) were acquired from Macklin (China). For photocrosslinking of SS-based precursor solutions, a visible-light photoinitiator system consisting of 0.5 mM $Ru(bpy)_3Cl_2$ and 10 mM $Na_2S_2O_8$ was used under 405 nm illumination. For GelMA, F127-DA and HAMA systems, LAP was employed at a final concentration of 0.3% (w/v) for photocrosslinking under visible light (405 nm). All solutions were prepared using DI water.

Fabrication of microgels via ATPS-based systems

Microgels were fabricated using an ATPS-based coaxial microfluidics setup. The system consisted of a digital syringe pump (Harvard Apparatus), a coaxial stainless steel nozzle (inner needle: outer diameter 0.63 mm, inner diameter 0.33 mm; outer needle: outer diameter 1.8 mm, inner diameter 1.55 mm), a UV-transparent collecting bath (6 cm diameter, filled with 5 mL of DI water or continuous phase), and an adjustable UV light source (Omnicure S2000, 360–480 nm, intensity 10 mW/cm^2, exposure time 3 min).

The dispersed phase consisted of a prepolymer solution composed of GelMA (10% w/v), photoinitiator LAP (0.3% w/v), and, when applicable, PEO (1% w/v, Mw = 300 kDa) as a sacrificial porogen for pore formation. For Janus microgels, two distinct prepolymer solutions were co-injected through a custom-built Y-shaped inner needle.

The continuous phase was a dextran aqueous solution (20% w/v, Mw = 500 kDa, Sigma-Aldrich), which provided interfacial stabilization and controlled the droplet shape through viscous shear and Rayleigh-Plateau instability. Both phases were loaded into separate 10 mL syringes and delivered through the coaxial nozzle using a syringe pump at precisely controlled flow rates (dispersed phase, 1 μL/min; continuous phase, 40 μL/min). The droplet formation regimen was tuned by adjusting the flow rate ratio and viscosity of each phase.

Spherical microgels were produced by allowing droplet formation at the outlet (15 cm) of the coaxial needle, followed by downstream UV (intensity 10 mW/cm^2, exposure time 3 min) crosslinking under continuous flow in the collection bath. Fibrous microgels were generated by repositioning the UV light source (intensity 10 mW/cm^2, exposure time 3 min) upstream (7 cm) to crosslink the jet prior to droplet breakup. Porous microgels were fabricated by incorporating sacrificial PEO (1% w/v) into the GelMA (10% w/v) phase, followed by UV (intensity 10 mW/cm^2, exposure time 3 min) curing and subsequent washing (3× with DI water, 10 min each) to remove the PEO and generate microporosity. CPGMs were prepared by incorporating 5% (w/v) COS into the GelMA solution prior to microgel formation. When applied at a working concentration of 10% (w/v), the COS content in the final system was 0.5% (w/v). Janus microgels were formed by parallel laminar flow of two GelMA-based prepolymer solutions delivered simultaneously through a dual-channel inner needle (channel dimensions: 0.21 mm × 0.21 mm), enabling the formation of biphasic droplets prior to photocrosslinking.

The size and morphology of microgels were characterized using optical microscopy (Nikon Eclipse Ti) and confocal laser scanning microscopy (Carl Zeiss LSM 880), and image analysis was performed using ImageJ.

Tunable morphology and size control

The morphology and diameter of the microgels were tuned by varying (1) the flow rate ratio between inner and outer phases, (2) GelMA concentration, and (3) nozzle diameter. For example, increasing the outer dextran flow, reducing the GelMA concentration, or decreasing the inner diameter will reduce the droplet

diameter, while higher GelMA flow or concentration resulted in larger droplets. The system allowed precise control of microgel sizes ranging from 77 to 710 μm with a coefficient of variation (CV) below 10%.

Phase diagram characterization

To assess material versatility, phase diagrams for various combinations of hydrogel precursors (GelMA, HAMA, SS, and F127-DA) with dextran were constructed by varying component concentrations. The binodal curves were identified to delineate single- and two-phase regions, guiding the formulation of compatible ATPS compositions for droplet formation. In this study, the dextran concentration was fixed at 20% (w/v) with a constant flow rate of 40 μL/min and a LAP concentration at 0.3% (w/v), while three distinct precursor solutions were evaluated: 2% (w/v) HAMA (flow rate ratio, 1 μL/min), 6% (w/v) SS (flow rate ratio, 0.4 μL/min), and 20% (w/v) F127-DA (flow rate ratio, 0.4 μL/min), followed by downstream UV (intensity, 10 mW/cm^2, exposure time, 3 min) crosslinking under continuous flow in the collection bath.

SEM

The morphology and porosity of microgels were visualized using SEM (Hitachi SU8010). Samples were lyophilized, mounted onto stubs, and sputter coated with gold before imaging.

Degradation and swelling assessment

Lyophilized porous GelMA microsphere samples (10% w/v, $n = 3$) were weighed (W_0) and transferred to centrifuge tubes containing 1 mL of PBS solution with 2 U/mL collagenase type II. The mixtures were incubated on a thermostatic shaker at 37°C. Fresh collagenase solution was replenished daily. Samples were collected at predetermined time points (1, 3, 5, and 7 days), rinsed three times with DI water, lyophilized, and re-weighed (W_t). The degradation percentage (D) was calculated as follows:

$$D\% = \frac{W_0 - W_t}{W_0}.$$

Lyophilized porous GelMA microsphere samples (10% w/v, $n = 3$) were weighed (W_0) and immersed in PBS (pH 7.4) at 37°C. At predetermined time points up to 24 h, microgels were collected, excess surface water was removed using filter paper, and they were re-weighed (W_t). The swelling ratio was calculated as follows:

$$\text{Swelling ratio} = \frac{W_t - W_0}{W_0}.$$

Co-culture, encapsulation, and viability evaluation of cells

A549, HeLa, and HUVECs were obtained from the Cell Bank of the Chinese Academy of Sciences (Wuhan, China). All cells were cultured in high-glucose Dulbecco's modified Eagle medium (DMEM; Gibco) supplemented with 10% fetal bovine serum (FBS; Gibco) and 1% penicillin-streptomycin (100 U/mL penicillin and 100 μg/mL streptomycin, Gibco) under standard conditions (37°C, 5% CO_2, humidified atmosphere).

For co-culture experiments, cells were seeded in 24-well plates at a density of 4×10^4 cells/well and allowed to reach ~80% confluence. GelMA microgels (prepared as described above; 8% GelMA with 0.3% LAP) were sterilized by UV irradiation for 30 min and added directly to the monolayer cultures at a final concentration of approximately 500 microgels per well. Co-cultures were maintained for 1, 4, and 7 days, with medium changed every 2 days.

For encapsulation studies, A549 cells, HeLa cells, or HUVECs were suspended in GelMA prepolymer solution (8% w/v with 0.3% LAP) at a concentration of 2×10^6 cells/mL. The cell-GelMA mixture was loaded into a microfluidics chip to form monodisperse droplets and crosslinked by UV exposure (10 mW/cm^2, 360–480 nm, 30 s) to generate cell-laden microgels. The microgels were collected and cultured in 24-well ultra-low attachment plates (Corning) at a density of 500 microgels per well in 1 mL complete medium under the same incubation conditions.

At designated time points (days 1, 4, and 7), cell viability was assessed using a Live/Dead Viability/Cytotoxicity Kit (KeyGEN) according to the manufacturer's protocol. Briefly, samples were incubated with a solution of 2 μM calcein-AM and 2 μM ethidium homodimer-1 in PBS for 30 min at 37°C. Stained samples were imaged using confocal laser scanning microscopy (CLSM; Carl Zeiss LSM 880).

For proliferation analysis, monolayer cultures were treated with CCK-8 (Dojindo). At each time point, 100 μL of fresh medium containing 10% CCK-8 reagent was added per well and incubated for 2 h at 37°C. Absorbance was measured at 450 nm using a microplate reader (BioTek).

To assess cytoskeletal organization, encapsulated cells were fixed in 4% paraformaldehyde (PFA) for 15 min at room temperature, permeabilized with 0.1% Triton X-100 for 10 min, and blocked with 1% BSA for 30 min. Samples were stained with Alexa Fluor 488-conjugated phalloidin (1:100 dilution; Thermo Fisher Scientific) for 30 min and counterstained with DAPI (1 μg/mL) for 10 min. Imaging was performed using CLSM (Carl Zeiss LSM 880) at 40× or 63× oil immersion magnification. z stack and orthogonal reconstructions were performed using Zen software.

All experiments were repeated at least three times with independent biological replicates ($n = 3$).

Degradation test of CPGMs

The prepared CPGMs were immersed in three different solutions at once, including PBS, SGF, and SIF (pH 7). All three groups were incubated at 37°C. Finally, we evaluated the integrity of microspheres using CLSMs at a specified time of 1–48 h.

Analysis of the release of COS from CPGMs

The CPGMs were immersed in SGF or SIF (pH 7) for 0–48 h. The absorbance of the supernatant from each group was evaluated after filtering using an UV-visible spectrophotometer at 202 nm. Each experiment was performed in triplicate.

Bacterial strains and growth conditions

V. cholerae O1 El Tor strain El2382 was provided by Shanghai Municipal Centers for Disease Control and Prevention. The bacterial strains were grown in Luria-Bertani (LB) broth.

In vivo mouse model of *V. cholerae* infection

All animal experiments were conducted in accordance with protocols approved by the institutional animal care and use committee. Female C57BL/6 mice aged 6–8 weeks were administered an oral antibiotic cocktail comprising ampicillin, neomycin, metronidazole, and vancomycin (Sigma-Aldrich) once daily for 3 consecutive days (5 mg of each antibiotic per mouse per day) to deplete the gut microbiota. To ensure gastric emptying, food was withdrawn 20–24 h before bacterial challenge.

Prior to infection, mice were intragastrically given 50 μL of 8.5% (w/v) sodium bicarbonate immediately followed by 50 μL of a PBS bacterial suspension containing 10^9 colony-forming units (CFUs) and 10% CPGMs. Post inoculation, mice had free access to sterile water and antibiotic-free chow. 72 hours post infection, animals were anesthetized and euthanized via cervical dislocation. The small intestines were excised, rinsed three times with PBS, and weighed. Tissue samples were then homogenized in 0.5 mL PBS, serially diluted, and plated on LB agar to quantify bacterial colonization. The level of *in vivo* intestinal colonization was calculated as CFUs per gram of intestinal tissue. Additionally, an IVIS Spectrum imaging system (PerkinElmer) was employed to monitor intestinal retention over a 48-h period.

RT-qPCR analysis of *V. cholerae* virulence genes

RNA was extracted from small intestinal tissues using TRIzol reagent (Takara), and cDNA was synthesized using a PrimeScript RT Reagent Kit (Takara). RT-qPCR was performed on an ABI 7500 system using SYBR Green. Gene expression levels of tcpA, tcpP, toxR, and toxT were analyzed, and the rpoS gene (nonspecific enrichment) was used as a reference. All primer sequences used in the analysis are listed in Table S1.

Histological analysis

Intestinal tissues were fixed in 4% PFA, paraffin embedded, sectioned, and stained with H&E. Inflammation and villus structure were evaluated by blinded histological scoring. Colonic histological damage was scored from 0 to 6: 0 = no damage, 1 = hyperproliferation with irregular crypts and loss of goblet cells, 2 = mild to moderate crypt loss (10%–50%), 3 = severe crypt loss (50%–90%), 4 = complete crypt loss with intact surface epithelium, 5 = small to medium ulcers (<10 crypt widths), and 6 = large ulcers (≥10 crypt widths). Inflammatory cell infiltration was scored separately for the mucosa (0 = normal, 1 = mild, 2 = moderate, 3 = severe), submucosa (0 = normal, 1 = mild to moderate, 2 = severe) and muscle/serosa (0 = normal, 1 = moderate to severe). The total score ranged from 0 to 12, summing epithelial damage and inflammatory infiltration.[37]

Statistical analyses

All data are presented as mean ± SD unless otherwise stated. Statistical analyses were performed using GraphPad Prism 10.0. Experimenters were blinded to mouse group assignments during outcome assessment. Data collection was not randomized but conducted in parallel with appropriate controls. No animals or data points were excluded from analysis. For comparisons between two groups, unpaired two-tailed Student's *t* tests were used for normally distributed data; for comparisons among multiple groups, one-way or two-way analysis of variance (ANOVA) was applied, followed by post hoc multiple comparisons where applicable. The Mann-Whitney *U* test was used for nonparametric data. The assumption of normal distribution was made but not formally tested. Values with $p < 0.05$, 0.01, 0.001, or 0.0001 were considered statistically significant (*), highly significant (**), very highly significant (***), or extremely highly significant (****) respectively; n.s. indicates no significance.

RESOURCE AVAILABILITY

Lead contact

Further information and requests for resources and reagents should be directed to and will be fulfilled by the lead contact, Guosheng Tang (guoshengtang@gzhmu.edu.cn).

Materials availability

This study did not generate new unique reagents. The self-synthesized biomaterials (GelMA, HAMA, and SS) described in this study are available from the lead contact upon reasonable request.

Data and code availability

- All data supporting the findings of this study are available within the paper and its supplemental information. Original imaging data (including SEM, CLSM, and IVIS images) are available from the lead contact upon reasonable request. Raw data for cell viability, bacterial colonization, and phase diagram characterization are included in the paper's materials.
- No custom code was generated in this study.
- Any additional information required to reanalyze the data reported in this paper is available from the lead contact upon request.

ACKNOWLEDGMENTS

This work was supported by the National Natural Science Foundation of China (NSFC, 32201183).

AUTHOR CONTRIBUTIONS

Conceptualization, G.T.; methodology, J.W., Long Chen, and L.X.; investigation, C.X., Lijie Chen, and L.W.; visualization, Lijie Chen and L.W.; validation, Y.L. and Z.J.; supervision, G.T.; formal analysis, X.Q. and L.X.; funding acquisition, G.T.; project administration, G.T.; writing – original draft, J.W., Long Chen, and C.X.; writing – review and editing; Y.L., Z.J., L.D., M.X., and G.T.

DECLARATION OF INTERESTS

The authors declare no competing interests.

SUPPLEMENTAL INFORMATION

Supplemental information can be found online at https://doi.org/10.1016/j.xcrp.2026.103253.

Received: October 31, 2025
Revised: January 28, 2026
Accepted: March 18, 2026
Published: April 15, 2026

REFERENCES

1. Feng, Q., Li, D., Li, Q., Cao, X., and Dong, H. (2022). Microgel assembly: Fabrication, characteristics and application in tissue engineering and regenerative medicine. Bioact. Mater. *9*, 105–119.

2. Rojek, K.O., Ćwiklińska, M., Kuczak, J., and Guzowski, J. (2022). Microfluidic formulation of topological hydrogels for microtissue engineering. Chem. Rev. *122*, 16839–16909.

3. Xuan, L., Hou, Y., Liang, L., Wu, J., Fan, K., Lian, L., Qiu, J., Miao, Y., Ravanbakhsh, H., Xu, M., and Tang, G. (2024). Microgels for cell delivery in tissue engineering and regenerative medicine. Nano-Micro Lett. *16*, 218.

4. Caprio, N.D., Davidson, M.D., Daly, A.C., and Burdick, J.A. (2024). Injectable MSC spheroid and microgel granular composites for engineering tissue. Adv. Mater. *36*, e2312226.

5. Hou, Y., Xuan, L., Mo, W., Xie, T., Lara, J.A.R., Wu, J., Cai, J., Nazir, F., Chen, L., Yi, X., et al. (2025). Anisotropic microcarriers: fabrication strategies and biomedical applications. Adv. Mater. *37*, 2416862.

6. Feng, Q., Li, Q., Wen, H., Chen, J., Liang, M., Huang, H., Lan, D., Dong, H., and Cao, X. (2019). Injection and self-assembly of bioinspired stem cell-laden gelatin/hyaluronic acid hybrid microgels promote cartilage repair in vivo. Adv. Funct. Mater. *29*, 1906690.

7. Ma, T., Gao, X., Dong, H., He, H., and Cao, X. (2017). High-throughput generation of hyaluronic acid microgels via microfluidics-assisted enzymatic crosslinking and/or Diels–Alder click chemistry for cell encapsulation and delivery. Appl. Mater. Today *9*, 49–59.

8. Griffin, D.R., Weaver, W.M., Scumpia, P.O., Di Carlo, D., and Segura, T. (2015). Accelerated wound healing by injectable microporous gel scaffolds assembled from annealed building blocks. Nat. Mater. *14*, 737–744.

9. Liu, Z., Wu, J., Luo, Z., Hou, Y., Xuan, L., Xiao, C., Chang, J., Zhang, D., Zheng, G., Guo, J., et al. (2024). 3D Biofabrication of microporous hydrogels for tissue engineering. Adv. Healthc. Mater. *14*, 2403583.

10. Nih, L.R., Sideris, E., Carmichael, S.T., and Segura, T. (2017). Injection of microporous annealing particle (MAP) hydrogels in the stroke cavity reduces gliosis and inflammation and promotes NPC migration to the lesion. Adv. Mater. *29*, 1606471.

11. Gao, Y., and Ma, Q. (2022). Bacterial infection microenvironment-responsive porous microspheres by microfluidics for promoting anti-infective therapy. Smart Med. *1*, e20220012.

12. Yang, X., Wang, C., Wang, Q., Zhang, Z., Nie, W., and Shang, L. (2023). Armored probiotics for oral delivery. Smart Med. *2*, e20230019.

13. Zhao, Z., Wang, Z., Li, G., Cai, Z., Wu, J., Wang, L., Deng, L., Cai, M., and Cui, W. (2021). Injectable microfluidic hydrogel microspheres for cell and drug delivery. Adv. Funct. Mater. *31*, 2103339.

14. Li, W., Zhang, L., Ge, X., Xu, B., Zhang, W., Qu, L., Choi, C.-H., Xu, J., Zhang, A., Lee, H., and Weitz, D.A. (2018). Microfluidic fabrication of microparticles for biomedical applications. Chem. Soc. Rev. *47*, 5646–5683.

15. Moragues, T., Arguijo, D., Beneyton, T., Modavi, C., Simutis, K., Abate, A.R., Baret, J.-C., deMello, A.J., Densmore, D., and Griffiths, A.D. (2023). Droplet-based microfluidics. Nat. Rev. Methods Primers *3*, 32.

16. Chen, L., Yang, C., Xiao, Y., Yan, X., Hu, L., Eggersdorfer, M., Chen, D., Weitz, D.A., and Ye, F. (2021). Millifluidics, microfluidics, and nanofluidics: manipulating fluids at varying length scales. Mater. Today Nano *16*, 100136.

17. Annabestani, M., Esmaeili-Dokht, P., and Fardmanesh, M. (2020). A novel, low cost, and accessible method for rapid fabrication of the modifiable microfluidic devices. Sci. Rep. *10*, 16513.

18. Daly, A.C., Riley, L., Segura, T., and Burdick, J.A. (2019). Hydrogel microparticles for biomedical applications. Nat. Rev. Mater. *5*, 20–43.

19. Liu, H.T., Wang, H., Wei, W.B., Liu, H., Jiang, L., and Qin, J.H. (2018). A microfluidic strategy for controllable generation of water-in-water droplets as biocompatible microcarriers. Small *14*, 1801095.

20. Field, R.D., Jakus, M.A., Chen, X., Human, K., Zhao, X., Chitnis, P.V., and Sia, S.K. (2022). Ultrasound-responsive aqueous two-phase microcapsules for on-demand drug release. Angew. Chem. Int. Ed. Engl. *61*, e202116515.

21. Iqbal, M., Tao, Y., Xie, S., Zhu, Y., Chen, D., Wang, X., Huang, L., Peng, D., Sattar, A., Shabbir, M.A.B., et al. (2016). Aqueous two-phase system (ATPS): an overview and advances in its applications. Biol. Proced. Online *18*, 18.

22. Cao, Y., Chao, Y., and Shum, H.C. (2024). Affinity-controlled partitioning of biomolecules at aqueous interfaces and their bioanalytic applications. Adv. Mater. *36*, 2409362.

23. Teixeira, A.G., Agarwal, R., Ko, K.R., Grant-Burt, J., Leung, B.M., and Frampton, J.P. (2018). Emerging biotechnology applications of aqueous two-phase systems. Adv. Healthc. Mater. *7*, 1701036.

24. Chao, Y., and Shum, H.C. (2020). Emerging aqueous two-phase systems: from fundamentals of interfaces to biomedical applications. Chem. Soc. Rev. *49*, 114–142.

25. Wang, H., Liu, H., Zhang, X., Wang, Y., Zhao, M., Chen, W., and Qin, J. (2021). One-step generation of aqueous-droplet-filled hydrogel fibers as organoid carriers using an all-in-water microfluidic system. ACS Appl. Mater. Interfaces *13*, 3199–3208.

26. Zhu, K., Yu, Y., Cheng, Y., Tian, C., Zhao, G., and Zhao, Y. (2019). All-aqueous-phase microfluidics for cell encapsulation. ACS Appl. Mater. Interfaces *11*, 4826–4832.

27. Yu, Y., Wei, W., Wang, Y., Xu, C., Guo, Y., and Qin, J. (2016). Simple spinning of heterogeneous hollow microfibers on chip. Adv. Mater. *28*, 6649–6655.

28. Tang, G., Luo, Z., Lian, L., Guo, J., Maharjan, S., Garciamendez-Mijares, C.E., Wang, M., Li, W., Zhang, Z., Wang, D., et al. (2023). Liquid-embedded (bio)printing of alginate-free, standalone, ultrafine, and ultrathin-walled cannular structures. Proc. Natl. Acad. Sci. USA *120*, e2206762120.

29. Ding, T., Xiao, Y., Saiding, Q., Li, X., Chen, G., Zhang, T., Ma, J., and Cui, W. (2024). Capture and storage of cell-free DNA via bio-informational hydrogel microspheres. Adv. Mater. *36*, 2403557.

30. Chen, D., Ge, S., Zuo, L., Wang, S., Liu, M., and Li, S. (2020). Adjudin-loaded redox-sensitive paclitaxel-prodrug micelles for overcoming multidrug resistance with efficient targeted colon cancer therapy. Drug Deliv. *27*, 1094–1105.

31. Liu, Y., Wu, J., Liu, R., Li, F., Xuan, L., Wang, Q., Li, D., Chen, X., Sun, H., Li, X., et al. (2024). Vibrio cholerae virulence is blocked by chitosan oligosaccharide-mediated inhibition of ChsR activity. Nat. Microbiol. *9*, 2909–2922.

32. Zhu, P., and Wang, L. (2016). Passive and active droplet generation with microfluidics: a review. Lab Chip *17*, 34–75.

33. Sauret, A., and Shum, H.C. (2012). Beating the jetting regime. Int. J. Nonlin. Sci. Num. *13*, 351–362.

34. Utada, A.S., Fernandez-Nieves, A., Stone, H.A., and Weitz, D.A. (2007). Dripping to jetting transitions in coflowing liquid streams. Phys. Rev. Lett. *99*, 094502.

35. Cubaud, T., and Mason, T.G. (2008). Capillary threads and viscous droplets in square microchannels. Phys. Fluids *20*, 053302.

36. du Chatinier, D.N., Figler, K.P., Agrawal, P., Liu, W., and Zhang, Y.S. (2021). The potential of microfluidics-enhanced extrusion bioprinting. Biomicrofluidics *15*, 041304.

37. Wu, J., Liu, Y., Liu, R., Xiao, C., Xuan, L., Wu, L., Qian, J., Qin, X., Hou, Y., Xie, M., et al. (2025). Fishing out AIEC with FimH capturing microgels for inflammatory bowel disease treatment. Nat. Commun. *16*, 7924.

38. Bahroudi, M., Bakhshi, B., Soudi, S., and Najar-peerayeh, S. (2021). Immunomodulatory effects of mesenchymal stem cell-conditioned media on lipopolysaccharide of Vibrio cholerae as a vaccine candidate. Stem Cell Res. Ther. *12*, 564.

39. La, S., Abaidullah, M., Li, H., Cui, Y., Liu, B., and Shi, Y. (2025). Alfalfa polysaccharide alleviates colitis by regulating intestinal microbiota and the intestinal barrier against the TLR4/MyD88/NF-κB pathway. Nutrients *17*, 3001.